IEEE Access
Multidisciplinary ⋮ Rapid Review ⋮ Open Access Journal

Received 14 November 2022, accepted 17 December 2022, date of publication 20 December 2022,
date of current version 28 December 2022.

Digital Object Identifier 10.1109/ACCESS.2022.3230893

RESEARCH ARTICLE

Nonlinear Stability Analysis and Active Compensation of a Utility-Scale Single-Stage Grid-Connected PV System

MD. MIZANUR RAHMAN, (Member, IEEE),
AND YASSER ABDEL-RADY I. MOHAMED, (Fellow, IEEE)
Department of Electrical and Computer Engineering, University of Alberta, Edmonton, AB T6G 1HG, Canada

Corresponding author: Md. Mizanur Rahman (mrahman4@ualberta.ca)

This work was supported by the Canada First Research Excellence Fund as part of the University of Alberta's Future Energy Systems Research Initiative.

ABSTRACT This paper presents a comprehensive nonlinear stability analysis and active compensation method for a utility-scale single-stage grid-connected photovoltaic (PV) system. First, a describing function (DF)-based stability analysis is conducted considering the nonlinear dynamics of the incremental conductance (INC)-based maximum power point tracking (MPPT) algorithm and the effects of the PV generator operating point changes. Next, the analysis characterizes the impact of the MPPT sampling time and perturbation step size on oscillation magnitude and frequency. The study showed that a shorter sampling time and larger step size result in a faster response. However, an increase in the step size increases the oscillation magnitude; the latter does not change with the step size. Then, considering the INC-based MPPT nonlinear dynamics, the overall system's damping and oscillatory modes are characterized under different photovoltaic generator operating conditions and system parameters using the DF method. The study showed that the system stability is reduced when the photovoltaic generator operating point moves to the left of the maximum power point and with the reduction of the dc-link capacitance and ac-side filter inductance. Therefore, an active compensation method is proposed to reduce the oscillations and improve the stability and dynamic performance at different operating conditions and in the presence of the MPPT nonlinear dynamics. Finally, detailed nonlinear time-domain simulation results are presented to validate the analytical results and the effectiveness of the proposed compensation method under various operating conditions.

INDEX TERMS Active compensation, incremental conductance, limit cycle, MPPT parameters, nonlinear analysis, photovoltaic systems, voltage-source converter.

I. INTRODUCTION

In recent years, to lower the typical fossil fuel-based energy sources utilization, photovoltaic generators (PVGs) have been considered promising renewable energy sources [1]. Two-stage PV systems linked to a grid adopt a dc-dc converter, where the maximum power point tracking (MPPT) algorithm is implemented, and a dc-ac converter for power conditioning. The two-stage system offers advantages, such as flexible control, but suffers from lower reliability, higher cost, and lower efficiency [2]. In comparison, a single-stage PV system adopts a single-power stage, offering a compact and cost-effective design. Therefore, single-stage PV systems are commonly preferred in utility-scale applications [3].

There are two components in the PVG dynamics: the continuous part, which includes the PV dynamics, and the discrete part, which includes the MPPT algorithm [4]. The linearized small-signal model can be used for the continuous part; however, it cannot be applied for the discontinuous one, making the PV interconnected system's stability and

The associate editor coordinating the review of this manuscript and approving it for publication was Akshay Kumar Saha.

performance analysis challenging. The MPPT algorithm generates the reference dc-link voltage for a single-stage system [5], where the MPPT dynamics and rapid actions can challenge the dc-link voltage control. The capacitance of the dc-link capacitor plays a vital role in determining the stability margins of the overall PV system and in meeting the steady-state performance requirements [6], [7].

Due to uniformity and simple application, perturb and observe (P&O)-based MPPT algorithms are commonly used [8]. However, it has two main drawbacks: the operating point oscillates around the MPP, and the effectiveness is reduced when irradiance changes rapidly. The fixed perturbation step size can reduce the oscillations, but it takes more time to arrive at an MPP [9]. In contrast, in the incremental conductance (INC)-based MPPT algorithm, the perturbation stops when the MPP is reached. It is also often stated that the INC-based MPPT can track fast-changing irradiance better than the P&O [10], [11].

In [12] and [13], the PV model was linearized for small-signal analysis ignoring the discontinuous MPPT part. Additionally, the discrete part cannot be analyzed using linear methods such as Bode, Nyquist, and root locus analysis. Dynamic analysis and stabilization of PV-based multiple microgrids were performed in [14] without considering the MPPT dynamics. In [15], a linearized small-signal model was developed for the INC-based MPPT in the continuous-time domain. However, practical MPPT algorithms are implemented digitally. The effects of the step size of the P&O and INC-based MPPT algorithms were addressed in [16], [17], and [18], where a small-signal linearization technique was used. The studies mentioned above, however, neither developed a mathematical model for the INC-based MPPT controller nor analyzed its nonlinear effects on the system's oscillatory behavior.

In the literature, stability analysis of grid-connected PV systems has been carried out [12], [13], [19]. A state-space model of a two-stage PV system was used in [12] to study the effect of the front-end converter, dc-link capacitance, and control loop parameters on the voltage-source converter (VSC) performance. However, the nonlinear MPPT dynamics were not analyzed. In [21], a feedback linearization scheme was used to design the voltage and current controllers. It is reported that zero dynamics are stable for a three-phase single-stage PV system. However, the MPPT controller was ignored. The effect of the grid impedance on the stability of a grid-connected VSC was addressed, where grid strength, operating point variation, and control loop parameters effects were studied [20], [22]. However, these studies did not consider the PVG dynamics and MPPT nonlinearities. Additionally, in existing literature, the stability analysis is conducted considering the time-domain approximation, which cannot predict a limit cycle behavior of a critically stable system. Moreover, the dynamic performance enhancement considering the MPPT nonlinearity under various operating conditions is not reported.

The well-known small-signal analysis is applied to linearize continuous nonlinear dynamics in the time domain. The grid-connected PV system contains both continuous and discontinuous elements. Therefore, linear studies based on the Bode diagram, Nyquist plot, and root locus analysis are not applicable anymore. In linear systems, the requirement for a linear, critically stable system is rigorous, where the point $(-1, j0)$ in the s-plane must be crossed by the Nyquist curve. On the contrary, in nonlinear systems, the oscillation criterion is difficult to find using linear analysis tools, restricting some quantitative analyses [23]. In contrast, a describing function (DF) is a frequency-domain approximation that can characterize the nonlinear behavior of a critically stable system.

A few stability analysis studies have been conducted using the DF method [4], [24], [25]. In [24], the stability of a PV connected to a weak grid system was conducted using the DF. Considering the modified P&O method, a reference power generation loop was proposed; however, the power injected into the grid is constant and lower than the MPP power. In [24], no mathematical derivation was reported to model the limit cycle characteristics as a function of the MPPT perturbation step size and sampling time. Moreover, no compensation technique was reported to suppress oscillations and improve the dc- and ac-side dynamics. Additionally, the system's behavior under a wide range of operating points was not reported. In [25], a constant power generation loop was proposed, a stiff grid was considered, and the DF method was used as an analysis tool. However, the study is limited to the characterization of the limit cycle behavior, ignoring the effect of the MPPT sampling time, dc- and ac-side uncertainties, and input/output impedance interactions. Furthermore, a compensation technique to suppress low-frequency oscillations was not reported. In [31], a P&O-based power control loop was proposed to analyze the system's stability. The effect of the perturbation step size and filters was considered in the stability analysis. However, an analytical model for the MPPT was not developed, and techniques to improve the dynamic performance were not reported.

It is apparent from the preceding survey that the nonlinear stability analysis of grid-connected PV systems has the following drawbacks.

1) The DF-based analysis reported in the literature did not consider the INC-based MPPT parameter-dependent mathematical model to characterize the nonlinear system dynamics and determine the optimal MPPT parameters, and
2) To the best of the authors' knowledge, considering the discontinuity of the system, the literature did not develop an active stabilization method to suppress the oscillations and facilitate stability under a wide range of operating conditions.

Motivated by these shortcomings in the literature, this paper presents a comprehensive DF-based nonlinear stability analysis and active compensation method for a utility-scale

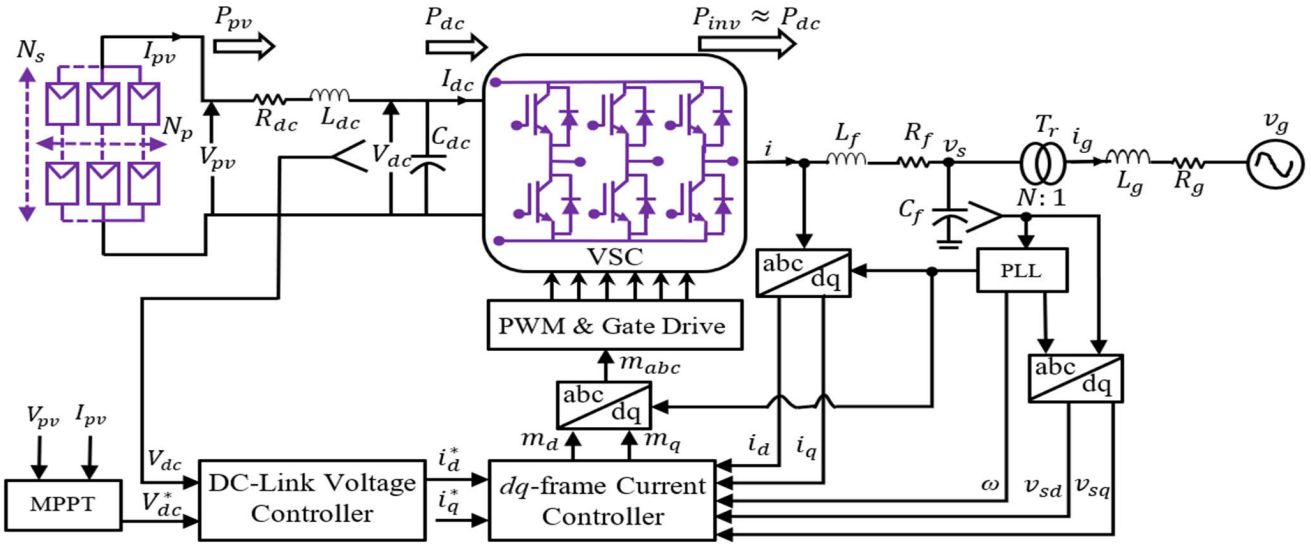

FIGURE 1. Utility-scale single-stage PV system.

single-stage grid-connected PV system. First, the INC-based MPPT analytical model is derived and used in the DF-based analysis to characterize the impact of the MPPT sampling time and perturbation step size on oscillation magnitude and frequency. Then, the limit cycle characteristics of the complete system dynamics are analyzed under different operating conditions and parameters. Furthermore, an active compensator is proposed to improve the damping and mitigate oscillations in the nonlinear system under various operating conditions. The contributions of this paper to the research field are as follows.

1) Developing an INC-based MPPT analytical model and using it in the DF-based analysis to characterize the impact of the MPPT sampling time and perturbation step size on oscillation magnitude and frequency,
2) Analyzing the oscillatory behavior of the complete utility-scale PV-VSC system considering the MPPT nonlinearity, PVG operating points, and changing system parameters, and
3) Developing an active compensator that reduces the oscillations and improves the stability and dynamic performance in the presence of the MPPT nonlinear dynamics.

The remainder of the paper is structured as follows. A detailed system model is developed in Section II for a utility-scale PV system. The DF and its principle for the stability study are presented in Section III. In Section IV, the mathematical model of the entire system is derived, considering the continuous and discrete parts as a function of the MPPT parameters. Section V presents a detailed stability analysis using the DF method. Section VI presents the proposed active compensation method. Finally, detailed nonlinear simulation results are presented in Section VII to verify the accuracy of the analytical results and the effectiveness of the proposed compensation method.

II. MODELING OF UTILITY-SCALE PV SYSTEM

The power circuit model of the complete system is presented in this section. Fig. 1 shows the configuration of a utility-scale grid-connected PV-VSC system. Table 1 in Appendix A gives the PV and dc-link parameters; the PV module parameters are selected from the Mitsubishi Electric PV-UD190MF5 datasheet [35]. The ac-side and control parameters are given in Appendix A - Tables 2 and 3, respectively, and they are selected following the standard guidelines of grid-connected converters [5], [36].

A. VSC-PV SYSTEM MODEL

Insulated-gate-bipolar-transistors (IGBT) with antiparallel diodes are used in the three-phase VSC, as shown in Fig. 1. The dc-cable, with resistance (R_{dc}) and inductance (L_{dc}), connects the PVG to the dc-link capacitor (C_{dc}). The interface reactor has a resistance (R_f) and inductance (L_f). The ac-side filter capacitance (C_f) attenuates the switching harmonics, and a step-up transformer connects the VSC to the grid system. The grid impedance has a resistance (R_g) and inductance (L_g). v_g represents the grid voltage. The mathematical model in the d-q frame with an angular velocity (ω) is given by

$$\left(R_f + sL_f\right) I_d - \omega L_f I_q = V_{id} - V_{sd} \tag{1}$$

$$\left(R_f + sL_f\right) I_q + \omega L_f I_d = V_{iq} - V_{sq} \tag{2}$$

$$sC_f V_{sd} - \omega C_f V_{sq} = I_d - \frac{1}{N} I_{gd} \tag{3}$$

$$sC_f V_{sq} + \omega C_f V_{sd} = I_q - \frac{1}{N} I_{gq} \tag{4}$$

$$\left(R_g + sL_g\right) I_{gd} - \omega L_g I_{gq} = \frac{1}{N} V_{sd} - V_{gd} \tag{5}$$

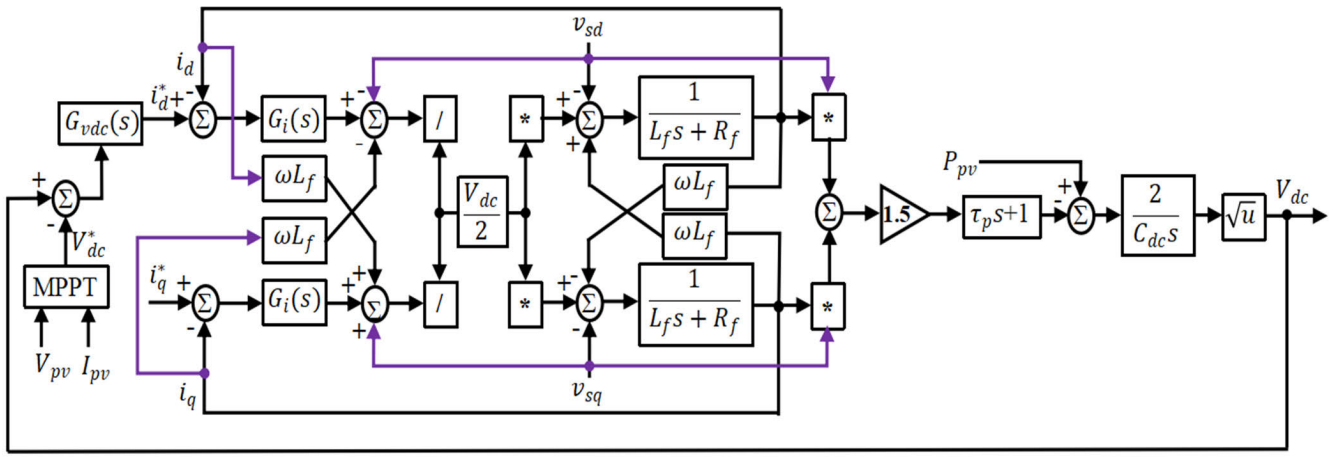

FIGURE 2. PV-VSC control diagram.

$$\left(R_g + sL_g\right) I_{gq} + \omega L_g I_{gd} = \frac{1}{N} V_{sq} - V_{gq} \tag{6}$$

$$sC_{dc} V_{dc} = I_{pv} - 1.5\left(M_d I_d + M_q I_q\right) \tag{7}$$

where $\left(V_{id}, V_{iq}\right)$, $\left(V_{sd}, V_{sq}\right)$, $\left(I_d, I_q\right)$, $\left(V_{gd}, V_{gq}\right)$, and $\left(I_{gd}, I_{gq}\right)$ are the inverter side d-q voltage, the voltage of the shunt capacitor (v_s), reactor current, the grid voltage $\left(v_g\right)$ and the grid current $\left(i_g\right)$, respectively. The VSC dc-side voltage is V_{dc}, PV current is I_{pv}, N is the transformer ratio, and s is the transformation operator in the Laplace domain.

Balanced ac voltages are considered for the mathematical model derivation in (1)-(7). The voltage V_{sd} is aligned to the d-axis and in a steady-state $V_{sq} = 0$. The PV array is structured with N_p parallel strings with N_s series-connected PV modules. The PV array current I_{pv} is given by

$$I_{pv} = N_p I_{ph} - N_p I_{rs}\left(exp\left\{\frac{q\left(V_{pv} + \left(N_s/N_p\right) R_s I_{pv}\right)}{N_s n_s A k T}\right\} - 1\right) - \frac{V_{pv} + \left(N_s/N_p\right) R_s I_{pv}}{\left(N_s/N_p\right) R_{sh}} \tag{8}$$

where the PV module equivalent series and shunt resistance is R_s and R_{sh}, respectively. The photon-generated current is I_{ph}, the p-n junction reverse saturation current is I_{rs}, the electric charge is q, the Boltzmann constant is k, and the diode ideality factor is A.

The dc cables are used to transmit power generated by the PV array to the VSC system, and cable dynamic is given by

$$L_{dc}\frac{dI_{pv}}{dt} + R_{dc} I_{pv} = V_{pv} - V_{dc} \tag{9}$$

where L_{dc} and R_{dc} is the resistance and inductance of the dc-cable, respectively [28].

B. PV-VSC CONTROL DESIGN

The PV-VSC control system is shown in Fig. 2, where the outer voltage controller generates the reference dc-link voltage (V_{dc}^*) through the MPPT algorithm. The ac current regulation is achieved through the inner current controller, and for unity power factor operation $i_q^* = 0$ [1]. The dc voltage controller $(G_{vdc}(s))$ processes the error signal between V_{dc} and V_{dc}^* and generates the active power generation reference current (i_d^*) as shown in Fig. 2. The signal after $G_{vdc}(s)$ is multiplied by a gain of "-1" to compensate for negative dc-power injection. A proportional-integral (PI) controller, $G_i(s)$, is used to regulate the currents i_d and i_q to their reference values i_d^* and i_q^*. The control loop dynamics are

$$I_d^* = -\left(V_{dc}^* - V_{dc}\right) G_{vdc}(s) \tag{10}$$

$$V_{id} = \left(I_d^* - I_d\right) G_i(s) - \omega L_f I_q + V_{sd} \tag{11}$$

$$V_{iq} = \left(I_q^* - I_q\right) G_i(s) + \omega L_f I_d + V_{sq} \tag{12}$$

where $G_{vdc}(s) = K_p^{vdc} + K_i^{vdc}/s$ and $G_i(s) = K_p^i + K_i^i/s$. K_p^{vdc} and K_p^i represent the proportional gains and K_i^{vdc} and K_i^i represent the integral gains, for $G_{vdc}(s)$ and $G_i(s)$, respectively.

The inner and outer current controllers are explained in the subsequent subsections.

1) INNER CURRENT CONTROL

The inner current control loop regulates i_d and i_q to their reference values to regulate the active and reactive power injection. For a fast current control response and to achieve high bandwidth (BW) characteristics of the closed-loop control system, the BW $(\omega_i = 1/\tau_i)$ is usually selected in the range of 10-20% of the switching frequency $(\omega_{sw} = 2\pi f_{sw})$ of the VSC, where τ_i is the time constant of the closed-loop current control [36]. The transfer function between the actual and reference current vectors $\vec{I}$ and $\vec{I}^*$ can be given by

$$\frac{\vec{I}}{\vec{I}^*} = \frac{K_p^i/L_f}{s + K_p^i/L_f} \tag{13}$$

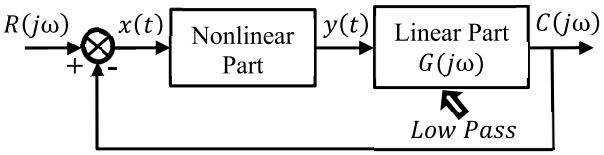

FIGURE 3. Typical structure of a nonlinear system.

From (13), $K_p^i = L_f/\tau_i$ and $K_i^i = R_f/\tau_i$ where $1/\tau_i$ is the BW (L_f/K_p^i) of the current control loop of the VSC.

2) DC-LINK VOLTAGE CONTROL

The voltage control loop is slower than the inner current controller loop. Therefore, to ensure that the phase delay of the current control loop at the gain cross-over frequency is negligible, the BW of the voltage control loop (ω_{vdc}) should be chosen adequately lower than the BW of the inner current control loop (ω_i) [2], [36]. The dc-side voltage control open-loop gain is given by

$$l_{vdc}(s) = \frac{2\left(1+\tau_p s\right)\left(K_p^{vdc} + K_i^{vdc}/s\right)}{C_{dc}s\left(1+\tau_i s\right)} \tag{14}$$

where $\tau_p = 2L_f P_{pv}^0/3\left(v_{sd}^0\right)^2$ is a positive time constant when the system operates in the inverting mode [3]. The gain of $G_{vdc}(s)$ can be computed as

$$\begin{aligned} K_p^{vdc} &= \frac{K_i^{vdc}\tan\theta_{vdc}}{\omega_{vdc}}; \\ K_i^{vdc} &= \frac{C_{dc}\omega_{vdc}^2\sqrt{1+(\tau_i\omega_{vdc})^2}}{\omega_{vdc}\sqrt{1+(\tan\theta_{vdc})^2}\sqrt{1+\left(\tau_p\omega_{vdc}\right)^2}} \\ \theta_{vdc} &= PM_{vdc} + \tan^{-1}(\tau_i\omega_{vdc}) - \tan^{-1}\left(\tau_p\omega_{vdc}\right) \end{aligned} \tag{15}$$

where PM_{vdc} and ω_{vdc} are the phase margin and cut-off frequency of the dc-side voltage control, respectively.

III. DESCRIBING FUNCTION METHOD-BASED LIMIT CYCLES CHARACTERIZATION

The DF method is a frequency-domain approximation. It can approximate the response characteristics of nonlinear systems, including the amplitude and frequency of oscillation [29]. In contrast, the linearization technique uses time-domain analysis for nonlinear elements [30]. The DF is concise and effective in analyzing stability, especially nonlinear dynamics. The control system structure is shown in Fig. 3 [31]. Assuming the input to the nonlinear part is sinusoidal as, $x(t) = Esin\omega t$ where E is the magnitude of the input signal and ω is the angular frequency. The nonlinear system output is $y(t)$. As the plant shows low-pass nature, higher-order harmonics are filtered out, resulting in only the fundamental output element. The complex ratio of amplitudes and phase angles between fundamental components of the output of a nonlinear element to the input sinusoid defines

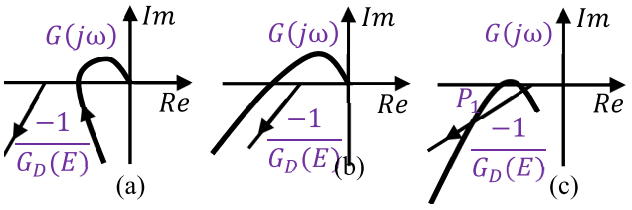

FIGURE 4. Stability analysis using the DF method: (a) stable state, (b) unstable state, and (c) critically stable state.

the DF as [30]

$$G_D(E) = \frac{Y_1(E,\omega)}{E}e^{j\theta_1} \tag{16}$$

From Fig. 3, the nonlinear element is $G_D(E)$, and the total linear components are in $G(j\omega)$. The closed-loop characteristic equation $G(j\omega) = \frac{-1}{G_D(E)}$ is fulfilled if $\frac{-1}{G_D(E)}$ graphically intersects $G(j\omega)$ Nyquist plot. The intersection point provides information on oscillation frequency (ω) and amplitude (E). The linear case where $G(j\omega)$ encloses the $(-1, j0)$ point in the Nyquist investigation can be continued to the nonlinear case where $G(j\omega)$ encircles the $\frac{-1}{G_D(E)}$. Therefore, the stability can be decided based on the corresponding position of $-1/G_D(E)$ and $G(j\omega)$ as [32]

(i) A stable system, as displayed in Fig. 4(a) if $-1/G_D(E)$ is not surrounded by $G(j\omega)$, whereas if it is surrounded, the system is unstable, as demonstrated in Fig. 4(b).

(ii) A critically stable system if two curves intersect, as shown in Fig. 4(c), and a limit cycle exists at the point of intersection.

If a disturbance is applied to a point, P_1, as shown in Fig. 4(c) such that if E is increased from E to $E + \Delta E$, $-1/G_D(E + \Delta E)$ shifts to the left of P_1, resulting in a stable system with reduced limit cycle amplitude. On the other hand, if E is decreased from E to $E - \Delta E$, $-1/G_D(E + \Delta E)$ shifts to the right of P_1, resulting in an unstable system. As a result, the limit cycle magnitude increases, and the operating point moves toward P_1, resulting in an asymptotically stable system.

IV. DF-BASED STABILITY ANALYSIS AS A FUNCTION OF MPPT PARAMETERS

The incremental conductance (INC)-based MPPT loop is nonlinear and discontinuous, creating periodic large-signal behaviors named limit cycles. But, the classical linearization technique (small-signal) cannot describe its properties, such as the magnitude and frequency of oscillation. Therefore, an MPPT parameter-dependent mathematical model is required to characterize the nonlinear MPPT behavior.

A. MATHEMATICAL MODEL OF MPPT CONTROLLER

Nowadays, digital implementation is preferred for MPPT algorithms. An MPPT parameter-dependent model of the entire system is shown in Fig. 5, which consists of a sign function and linear plant. Mathematically, an INC-based

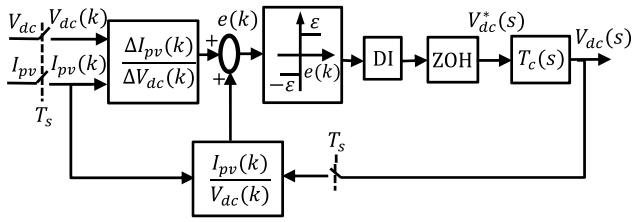

FIGURE 5. DF-based model of the system.

algorithm can be expressed as

$$\Longrightarrow \frac{1}{V_{dc}}\frac{dP_{pv}}{dV_{dc}} = \frac{I_{pv}}{V_{dc}} + \frac{dI_{pv}}{dV_{dc}} \Longrightarrow e = \frac{I_{pv}}{V_{dc}} + \frac{dI_{pv}}{dV_{dc}} \tag{17}$$

where the error signal (e) can be approximated in a discrete-time domain by applying the forward Euler method as

$$e(k) = \frac{I_{pv}(k)}{V_{dc}(k)} + \frac{\Delta I_{pv}(k)}{\Delta V_{dc}(k)} \tag{18}$$

At the MPP $e = 0$, the perturbation is unchanged. However, e is positive on the left and negative on the right side of the MPP. Therefore, a step size (ε) on the left of the MPP increases V_{dc}^*, whereas it decreases V_{dc}^* when it is on the right side of the MPP. Linearizing (18) around the MPP

$$e = e\left(V_{mpp}, I_{mpp}\right) + \frac{\partial e\left(V_{dc}, I_{pv}\right)}{\partial V_{dc}}\Big|_{MPP}\left(V_{dc} - V_{mpp}\right) + \frac{\partial e\left(V_{dc}, I_{pv}\right)}{\partial I_{pv}}\Big|_{MPP}\left(I_{pv} - I_{mpp}\right) \tag{19}$$

At the steady-state point $\left(V_{mpp}, I_{mpp}\right)$

$$\frac{\partial e\left(V_{dc}, I_{pv}\right)}{\partial V_{dc}}\Big|_{MPP} = \frac{-I_{MPP}}{V_{MPP}^2} \text{ and } \frac{\partial e\left(V_{dc}, I_{pv}\right)}{\partial i_{pv}}\Big|_{MPP} = \frac{1}{V_{mpp}} \tag{20}$$

From (19) and (20), the error signal is obtained as

$$e = \frac{-I_{MPP}}{V_{MPP}^2}\left(V_{dc} - V_{mpp}\right) + \frac{1}{V_{mpp}}\left(I_{pv} - I_{mpp}\right) \tag{21}$$

Linearizing the PV curve around the MPP by a tangent with a slope $-1/R_{MPP}$ results

$$I_{pv} - I_{mpp} = \frac{-1}{R_{MPP}}\left(V_{dc} - V_{mpp}\right) \tag{22}$$

Substituting (22) into (21) describes the MPPT action as

$$\tilde{e} = k_m \tilde{V}_{dc} \tag{23}$$

where, $k_m = \frac{-2}{V_{mpp}R_{MPP}}$.

B. DF-BASED ANALYSIS AS A FUNCTION OF MPPT PARAMETERS

The DF of the relay function, shown in Fig. 5, is $G_D(E) = \frac{4\varepsilon}{\pi E}$. The error is adjusted and processed by a digital integrator (DI). For digital implementation, the DI is represented by the forward Euler form of $T_s/(z-1)$. The discrete-time signal can be transformed into a continuous counterpart using a zero-order hold (ZOH) block to generate V_{dc}^*, where $G_{ZOH}(s) = 1 - e^{-sT_s}/sT_s$.

From (7),

$$sC_{dc}V_{dc} = I_{pv} - 1.5\frac{V_{sd}}{V_{dc}}I_d = I_{pv} + \alpha_1 I_d \tag{24}$$

where $\alpha_1 = 1.5V_{sd}/V_{dC}$. Linearizing (24) around the operating points and considering $\alpha_2 = -\frac{\partial I_{pv}}{\partial V_{dc}}\Big|_{(I_{pv0}, V_{dc0}, I_{d0})}$,

$$\frac{V_{dc}(s)}{I_d(s)} = \frac{\alpha_1}{sC_{dc} + \alpha_2} \tag{25}$$

The outer controller output (I_d^*) is processed by a current controller to generate I_d. Finally, using (25), the transfer function between $V_{dc}(s)$ and $V_{dc}^*(s)$ can be obtained as

$$T_c(s) = \frac{V_{dc}(s)}{V_{dc}^*(s)} = \frac{\alpha_1 K_i^{vdc}/\alpha_2\tau_i}{s^2 + \left(1/\tau_i\right)s + \alpha_1 K_i^{vdc}/\alpha_2\tau_i} \tag{26}$$

Comparing the system with a second-order system results in

$$T_c(s) = \frac{V_{dc}(s)}{V_{dc}^*(s)} = \frac{1}{2\tau_i^2 s^2 + 2\tau_i s + 1} \tag{27}$$

The linear part transfer function with $z = e^{sT_s}$ results

$$G(s) = \frac{k_m\left(1 - e^{-sT_s}\right)}{sT_s\left(e^{sT_s} - 1\right)\left(2\tau_i^2 s^2 + 2\tau_i s + 1\right)} = \frac{k_m\left(1 - sT_s\right)}{sT_s\left(2\tau_i^2 s^2 + 2\tau_i s + 1\right)} \tag{28}$$

Based on the relationship of $G(j\omega) = \frac{-1}{G_D(E)}$ and substituting the real and imaginary components results

$$E = \frac{4\varepsilon k_m}{\pi T_s}\left(\tau_i + T_s\right) \text{ and } \omega^2 = \frac{1}{2\tau_i\left(\tau_i + T_s\right)} \tag{29}$$

From (29), the limit cycle magnitude (E) depends on ε. Also, a higher value of the MPPT sampling time (T_s) results in a lower oscillation frequency and vice-versa. From Fig. 6(a), if T_s increases, the intersection point of $G(j\omega)$ and $\frac{-1}{G_D(E)}$ moves towards the right from A to C. Therefore, the dominant poles move closer to the imaginary axis, resulting in a slower response. Fig. 6(b) demonstrates a critically stable system; when ε increases from 0.25 to 0.75 V, the oscillation magnitude increases, but there is a slight change in the oscillation frequency. The oscillation magnitude and frequency for different sampling times can be calculated as

$$\begin{cases} A_A = .022 \text{ W} \\ A_B = .018 \text{ W} \\ A_C = .017 \text{ W} \end{cases} \quad \begin{cases} \omega_A = 378 \text{ rad/s} \\ \omega_B = 289 \text{ rad/s} \\ \omega_C = 213 \text{ rad/s} \end{cases}$$

$$\begin{cases} A_D = 1000 \text{ W} \\ A_E = 550 \text{ W} \\ A_F = 100 \text{ W} \end{cases} \quad \begin{cases} \omega_D = 86 \text{ rad/s} \\ \omega_E = 74 \text{ rad/s} \\ \omega_F = 62 \text{ rad/s} \end{cases}$$

For smaller values of ε and larger values of T_s, the dominant pole moves close to the imaginary axis resulting in a slower response with a higher settling time, as shown in Fig. 7. However, larger values of ε result in a faster response, which increases the oscillation amplitude.

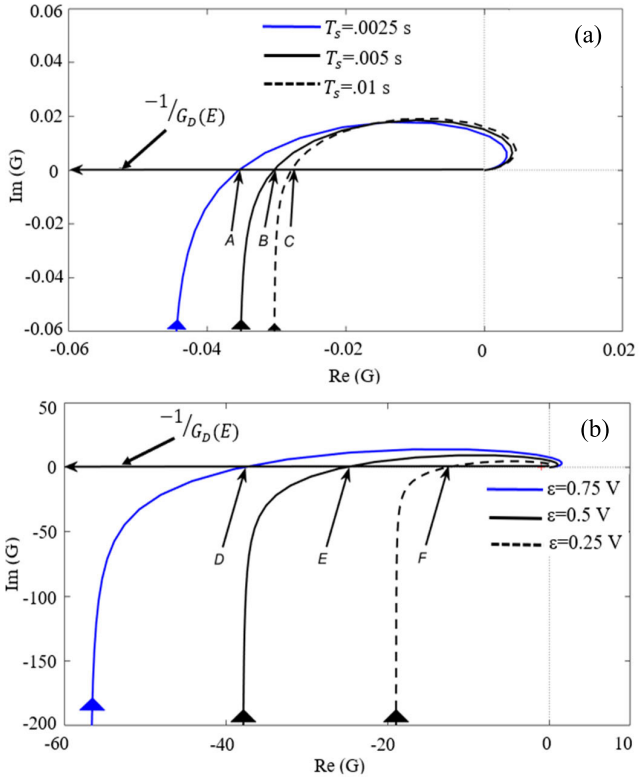

FIGURE 6. The Nyquist and DF diagrams: (a) effect of T_S and (b) effect of ε.

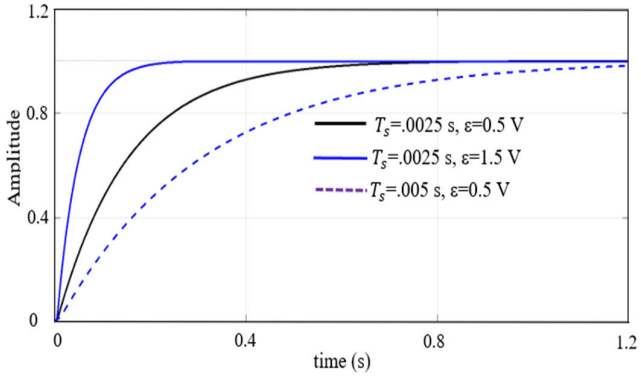

FIGURE 7. Effect of MPPT parameters on system performance.

V. DESCRIBING FUNCTION-BASED STABILITY ANALYSIS OF A PV-VSC SYSTEM

The transfer function of the entire system is determined, and a DF-based comprehensive analysis is carried out to assess the oscillatory behavior under different operating conditions and varying system parameters.

A. TRANSFER FUNCTION OF THE PV-VSC SYSTEM

Linearizing the PV power and separating the linearized quantities gives $\Delta P_{PV} = V^0_{PV}\Delta I_{PV} + I^0_{PV}\Delta V_{PV}$. Finally, at the MPP, for N_p parallel strings with N_s series PV modules

$$\Delta I_{PV} = -\frac{N_p}{N_s}\frac{I_{MPP}}{V_{MPP}}\Delta V_{PV} = K_{PV}\Delta V_{PV} \tag{30}$$

where, $K_{PV} = -\frac{N_p}{N_s}\frac{I_{MPP}}{V_{MPP}}$.

From (1), (2), and (7),

$$\Delta I_d = \frac{\omega L_f \Delta I_q + V^0_{dc}\Delta M_d + M^0_d \Delta V_{dc}}{sL_f + R_f} \tag{31}$$

$$\Delta I_q = \frac{-\omega L_f \Delta I_d + V^0_{dc}\Delta M_q + M^0_q \Delta V_{dc}}{sL_f + R_f} \tag{32}$$

$$\Delta V_{dc} = \frac{-1.5\left(M^0_d\Delta I_d + I^0_d\Delta M_d + M^0_q\Delta I_q\right)}{C_{dc}s - K_{PV}} \tag{33}$$

From (1), (2), and (31)-(33), considering $R_f \approx 0$,

$$\Delta I_d = A_1\Delta M_d + A_2\Delta M_q \tag{34}$$

$$\Delta I_q = A_3\Delta M_d + A_4\Delta M_q \tag{35}$$

$$\Delta V_{dc} = A_5\Delta M_d + A_6\Delta M_q \tag{36}$$

where the equation can be derived, as shown at the bottom of next page. From the control diagram shown in Fig. 2,

$$\Delta M_d = \left[\left(\Delta V_{dc} - \Delta V^*_{dc}\right)G_{vdc}(s) - \Delta I_d\right]G_i(s) \tag{37}$$

$$\Delta M_q = -\Delta I_q G_i(s) \tag{38}$$

From (34)-(38),

$$\Delta I_q = \frac{A_3}{1 + A_4 G_i(s)} = A_7\Delta M_d \tag{39}$$

$$\Delta I_d = \left[A_1 - A_2 G_i(s) A_7\right]\Delta M_d = A_8\Delta M_d \tag{40}$$

$$\Delta V_{dc} = \left[A_5 - A_6 G_i(s) A_7\right]\Delta M_d = A_9\Delta M_d \tag{41}$$

Substituting the values of ΔI_d, ΔI_q and ΔV_{dc} in (37) results

$$\frac{\Delta V_{dc}}{\Delta V^*_{dc}} = G(s) = \frac{A_9 G_{vdc}(s) G_i(s)}{G_{vdc}(s) G_i(s) A_9 - A_8 G_i(s) - 1} \tag{42}$$

Equation (42) is used to analyze the limit cycle characteristics of the PV-VSC system using the DF method, where the system parameters are listed in Appendix A.

B. OVERALL PV-VSC SYSTEM STABILITY STUDY

Fig. 8 shows the Nyquist diagram of the entire system dynamics at different PVG operating conditions and varying system parameters. Fig. 8(a) shows that the system remains stable at the MPP and points on the right side of the MPP. However, movement of the operating point to the left of the MPP (voltage lower than the MPP voltage) greatly influences the oscillation amplitude and suffers from low-frequency stability problems. As a result, the oscillation amplitude and frequency on the left side of the MPP are 5.1 kW and 205 rad/s (equivalent frequency is 33 Hz), respectively. Reduced dc-link capacitor (C_{dc}) with operating points on the left side of the MPP results in a critically stable system with increasing oscillation magnitude, as shown in Fig. 8(b). For $C_{dc} = 1000\ \mu$F, the oscillation magnitude and frequency are 3.7 kW and 94.2 rad/s, respectively. The effect of changing the ac-side filter inductance on the system behavior is shown in Fig. 8(c). As L_f changes from 0.1 to 0.5 mH, the system becomes stable. However, for $L_f = 0.1$ mH, the oscillation is more prominent and results in a critically stable system with an oscillation magnitude and frequency of 22.2 kW and 114 rad/s, respectively.

VI. PROPOSED ACTIVE COMPENSATOR STRATEGY FOR THE PV-VSC SYSTEM

The DF-based analysis showed that the grid-connected PV system might suffer high oscillations due to the nonlinear MPPT dynamics and changes in the PVG operating conditions and system parameters. To overcome this difficulty in a simple way, this paper presents an effective active compensation technique that reduces the dc-side impedance of the VSC in a way that minimizes undesirable interactions between the VSC and MPPT controller. The proposed active compensator modifies the converter impedance by injecting a compensation signal in the d-axis control structure of the VSC interface to maintain stability and high damping capability at different operating conditions and in the presence of MPPT nonlinearity. In a PV-VSC system, the dc-link voltage (V_{dc}) is usually measured. Therefore, it is used in the proposed compensator to map the voltage dynamics to the closed-loop system to achieve the desired dynamics [34].

A. VSC DC-SIDE IMPEDANCE DERIVATION

From the power balance equation

$$V_{dc}I_{dc} = 1.5\left(V_{id}I_d + V_{iq}I_q\right) \tag{43}$$

The relationship between $I_d - V_{sd}$ and $V_{id} - V_{sd}$ can be expressed in a small-signal sense as

$$\Delta I_d = \left(sC_f + \frac{1}{N^2}\cdot\frac{1}{Z_g}\right)\Delta V_{sd} \tag{44}$$

$$\Delta V_{id} = \left[1 + \left(R_f + sL_f\right)\left(sC_f + \frac{1}{N^2}\cdot\frac{1}{Z_g}\right)\right]\Delta V_{sd} \tag{45}$$

From (10) and (11),

$$\Delta V_{sd} = \frac{M_d^0 + G_{vdc}(s)G_i(s)}{\left(R_f + sL_f + G_i(s)\right)\left(sC_f + \frac{1}{N^2}\cdot\frac{1}{Z_g}\right)}\Delta V_{dc} \tag{46}$$

From (43),

$$V_{dc}^0\Delta I_{dc} + I_{dc}^0\Delta V_{dc} = 1.5\left(V_{id}^0\Delta I_d + I_d^0\Delta V_{id} + V_{iq}^0\Delta I_q + I_q^0\Delta V_{iq}\right) \tag{47}$$

From the voltage orientations, the q-axis inverter output voltage is zero and $I_q^0 = 0$ for unity power factor operation. From (44), (45), and (47),

$$\begin{aligned} V_{dc}^0\Delta I_{dc} + I_{dc}^0\Delta V_{dc} &= \frac{1.5}{N^2\left(R_g + sL_g\right)} \\ &\times \left[I_d^0N^2L_gL_fC_fs^3 + \left\{N^2L_gC_f\left(V_{id}^0 + I_d^0R_f\right)\right.\right. \\ &\left. + I_d^0N^2L_fR_gC_f\right\}s^2 + \left\{N^2R_gC_f\left(V_{id}^0 + I_d^0R_f\right)\right. \\ &\left.\left. + I_d^0\left(L_f + N^2L_g\right)\right\}s + V_{id}^0 + I_d^0\left(R_f + N^2R_g\right)\right]\Delta V_{sd} \end{aligned} \tag{48}$$

From (46) and (48), the small-signal dc-side impedance (ΔZ_{dc}) can be calculated as

$$\Delta Z_{dc} = \frac{\Delta V_{dc}}{\Delta I_{dc}} = \frac{V_{dc}^{02}\left(\beta_5s^5 + \beta_4s^4 + \beta_3s^3 + \beta_2s^2 + \beta_1s\right)}{\alpha_5s^5 + \alpha_4s^4 + \alpha_3s^3 + \alpha_2s^2 + \alpha_1s + \alpha_0} \tag{49}$$

where the coefficients α_5, α_4, α_3, α_2, α_1, α_0, β_5, β_4, β_3, β_2, and β_1 are listed in Appendix B.

$$A_1 = \frac{L_fC_{dc}V_{dc}^0s^2 - L_f\left(1.5I_d^0M_d^0 + K_{PV}V_{dc}^0\right)s + \left(1.5M_q^{02}V_{dc}^0 - 1.5I_d^0M_q^0\omega L_f\right)}{L_f^2C_{dc}s^3 - L_f^2K_{PV}s^2 + \left(C_{dc}\omega^2L_f^2 + 1.5M_d^{02}L_f + 1.5M_q^{02}L_f\right)s - K_{PV}\omega^2L_f^2}$$

$$A_2 = \frac{\omega L_fC_{dc}V_{dc}^0s - \left(\omega L_fK_{PV}V_{dc}^0 + 1.5M_d^0M_q^0V_{dc}^0\right)}{L_f^2C_{dc}s^3 - L_f^2K_{PV}s^2 + \left(C_{dc}\omega^2L_f^2 + 1.5M_d^{02}L_f + 1.5M_q^{02}L_f\right)s - K_{PV}\omega^2L_f^2}$$

$$A_3 = \frac{-\left(\omega L_fC_{dc}V_{dc}^0 + 1.5I_d^0M_q^0L_f\right)s + 1.5I_d^0M_d^0\omega L_f + \omega L_fK_{PV}V_{dc}^0 - 1.5M_d^0M_q^0V_{dc}^0}{L_f^2C_{dc}s^3 - L_f^2K_{PV}s^2 + \left(C_{dc}\omega^2L_f^2 + 1.5M_d^{02}L_f + 1.5M_q^{02}L_f\right)s - K_{PV}\omega^2L_f^2}$$

$$A_4 = \frac{L_fC_{dc}V_{dc}^0s^2 - L_fK_{PV}V_{dc}^0s + 1.5M_d^{02}V_{dc}^0}{L_f^2C_{dc}s^3 - L_f^2K_{PV}s^2 + \left(C_{dc}\omega^2L_f^2 + 1.5M_d^{02}L_f + 1.5M_q^{02}L_f\right)s - K_{PV}\omega^2L_f^2}$$

$$A_5 = \frac{-1.5\left(L_f^2I_d^{02}s^2 + M_d^0V_{dc}^0L_fs + I_d^0\omega^2L_f^2 - M_q^0V_{dc}^0\omega L_f\right)}{L_f^2C_{dc}s^3 - L_f^2K_{PV}s^2 + \left(C_{dc}\omega^2L_f^2 + 1.5M_d^{02}L_f + 1.5M_q^{02}L_f\right)s - K_{PV}\omega^2L_f^2}$$

$$A_6 = \frac{-1.5\left(M_q^0V_{dc}^0L_fs + M_d^0V_{dc}^0\omega L_f\right)}{L_f^2C_{dc}s^3 - L_f^2K_{PV}s^2 + \left(C_{dc}\omega^2L_f^2 + 1.5M_d^{02}L_f + 1.5M_q^{02}L_f\right)s - K_{PV}\omega^2L_f^2}$$

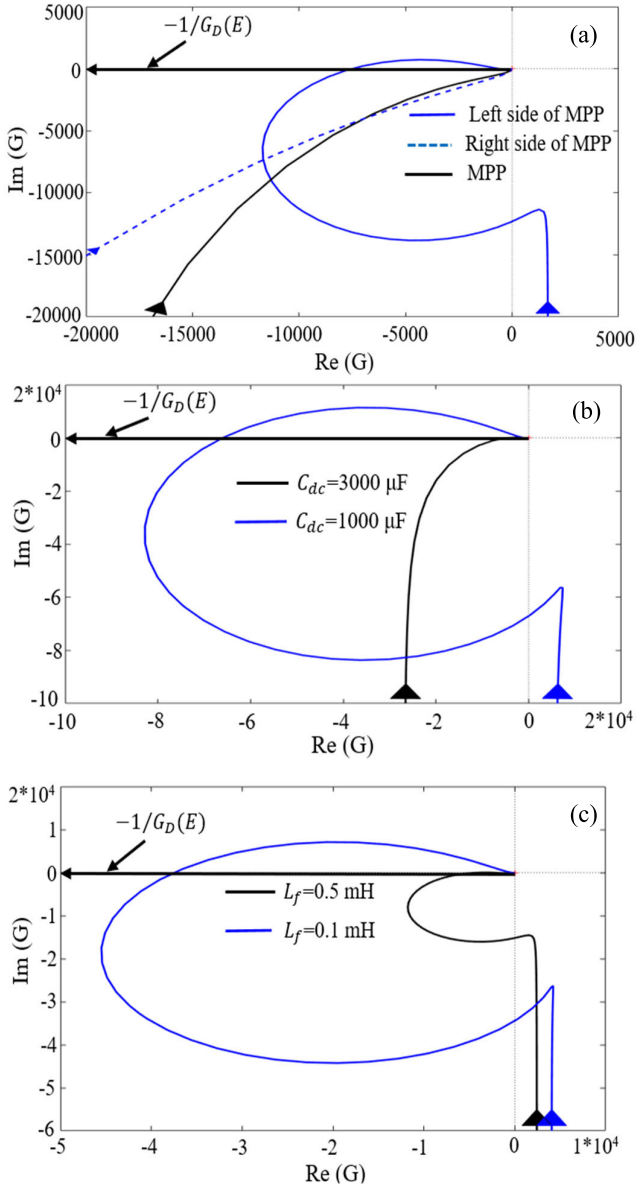

FIGURE 8. Low-frequency stability study: (a) effect of changes in the PVG operating points, (b) effect of C_{dc} and (c)) effects of L_f.

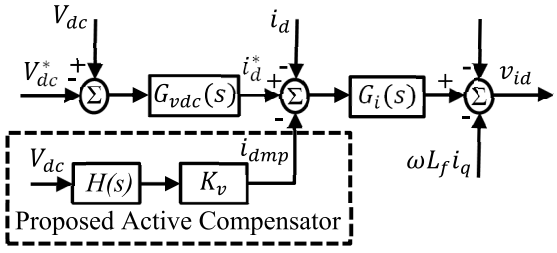

FIGURE 9. Schematic diagram of the proposed active compensator.

B. PROPOSED ACTIVE COMPENSATOR

A simple yet effective active compensation technique (shown in Fig. 9) is proposed to reduce the oscillations and improve the stability of the PV-VSC system under different operating conditions. In this method, a scaled version of the measured dc-link voltage (V_{dc}) is scaled by a gain (K_v) and processed by a first-order low-pass filter with a transfer function $H(s)$ to generate the damping signal (i_{dmp}). The latter is injected into the d-axis control channel of the interfacing VSC. The low-pass filter has a cut-off frequency of ω_c. The damping signal can be expressed as

$$i_{dmp} = K_v \frac{\omega_c}{s+\omega_c} V_{dc} \tag{50}$$

The compensators parameter are designed by varying ω_c and K_v to achieve reduced voltage oscillations in the dc-link. The optimal selection of the compensator parameters ensures high damping and reduces unsatisfactory interactions with the MPPT controller. The control law in (11) with the proposed compensator can be expressed as

$$v_{id} = \left(i_d^* - i_d - i_{dmp}\right) G_i(s) - \omega L_f i_q + v_{sd} \tag{51}$$

The modified $\Delta V_{sd} - \Delta V_{dc}$ relationship can be expressed as

$$\Delta V_{sd} = \frac{M_d^0 + G_{vdc}(s)\, G_i(s) + G_i(s)\, K_v \frac{\omega_c}{s+\omega_c}}{\left(R_f + sL_f + G_i(s)\right)\left(sC_f + \frac{1}{N^2}\cdot\frac{1}{Z_g}\right)} \Delta V_{dc} \tag{52}$$

From (48) and (52), the modified dc-side impedance (ΔZ_{dc-com}) with the proposed compensator can be determined as

$$\begin{aligned}\Delta Z_{dc-com} &= \frac{\Delta V_{dc}}{\Delta I_{dc}} \\ &= \frac{V_{dc}^{02}\left(A_6 s^6 + A_5 s^5 + A_4 s^4 + A_3 s^3 + A_2 s^2 + A_1 s\right)}{B_6 s^6 + B_5 s^5 + B_4 s^4 + B_3 s^3 + B_2 s^2 + B_1 s + B_0}\end{aligned} \tag{53}$$

where the coefficients $A_6, A_5, A_4, A_3, A_2, A_1, A_0, B_6, B_5, B_4, B_3, B_2, B_1$ and B_0 are listed in Appendix B.

Fig. 10 shows the profile of the converter impedance with different cut-off frequencies and gains. The proposed compensator reduces the converter impedance in a wide range of frequencies corresponding to the dc-link voltage oscillations originating from the nonlinear MPPT dynamics. The reduced

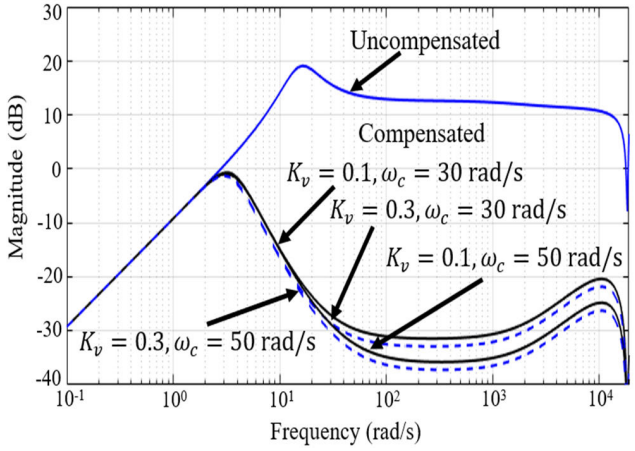

FIGURE 10. Converter impedance reduction with the proposed compensator.

impedance reduces interactions with the nonlinear MPPT controller and yields higher damping capability and reduced oscillations than the uncompensated system.

VII. EVALUATION RESULTS

Detailed nonlinear time-domain simulations of the PV-VSC system depicted in Fig. 1 are conducted to evaluate the analytical results and the performance of the proposed active damping scheme. The simulation study is implemented in the Matlab/Simulink environment using the switching models of the VSC. A sample time of 20 μs is used for the discrete-type simulation. The complete system and control parameters are listed in Appendix A. The model is tested under a wide range of operating conditions. The following simulation scenarios are reported:

1) Influence of MPPT parameters.
2) Operation under varying dc-link capacitor and filter inductor.
3) Operation of the uncompensated PV-VSC system.
4) Operation with the proposed compensator.
5) Operation under fault.
6) Operation under grid-voltage parameter variation.
7) Operation under a weak grid condition.

A. INFLUENCE OF MPPT PARAMETERS

Fig. 11 shows the dc-link voltage (V_{dc}) response under changing MPPT parameters. If the step size (ε) increases from 0.25 to 0.75 V at $t = 1.5$ s (with sampling time, $T_s = 0.02$ s), the dc-link voltage oscillation increases, as shown in Fig. 11(a), verifying the higher oscillation magnitude revealed in the theoretical analysis presented in Section IV. The oscillation amplitude and frequency are 1.0 kV and 14.25 Hz (low-frequency oscillation), respectively, for $\varepsilon = 0.75$ V. However, the limit cycle frequency does not change. Fig. 11(b) presents the V_{dc} response when T_s changes from 0.001 to 0.01 s. The smaller value of the MPPT sampling time gives a faster transient response, as illustrated in Fig. 11(b). Therefore, the MPPT parameters play an important role in assessing the complete dynamic behavior of a grid-connected PV-VSC system.

B. OPERATION UNDER VARYING DC-LINK CAPACITOR AND FILTER INDUCTOR

This case study demonstrates the effects of the dc-link capacitance (C_{dc}) and filter inductance (L_f) on the dc-link votlage dynamics. If C_{dc} changes from 3000 to 1000 μF, with the PVG operating point moving to the left of the MPP, higher oscillations are yielded, as shown in Fig. 12(a). Fig. 12(b) shows the effect of C_{dc} when a disturbance is enforced at $t = 1.0$ s with a duration of 0.06 s by connecting a shunt resistance. Under the disturbance, if C_{dc} changes from 3000 to 5000 μF, V_{dc} suffers from higher oscillations, as demonstrated in Fig. 12(b). If L_f decreases, more oscillations are seen when the PVG operates on the left of the MPP, as shown in Fig. 12(c). The oscillation frequencies are 110 and 92 rad/s when L_f changes from

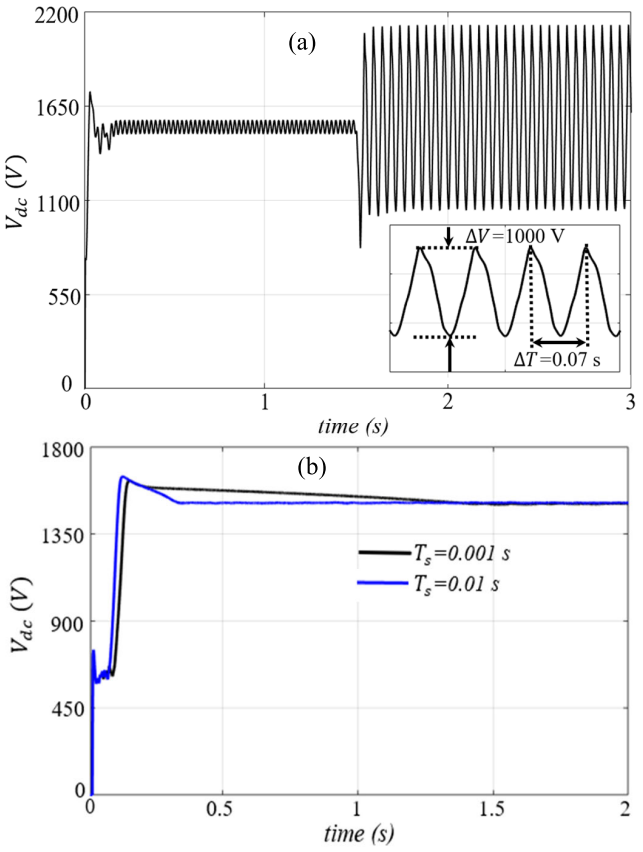

FIGURE 11. DC-link Voltage response: (a) the effect of ε and (b) the effect of T_S.

0.1 to 0.5 mH, respectively. Therefore, it is clear that different selections of system parameters might introduce oscillations at changing PVG operating conditions.

C. UNCOMPENSATED PV-VSC SYSTEM

Fig. 13 shows the nonlinear time-domain uncompensated V_{dc} and injected ac current (I_d) responses for changing dc-link voltage reference. The change in the operating point yields a critically stable system. V_{dc} oscillates with a frequency of 42.9 Hz for an operating point of the left side of the MPP, as shown in Fig. 13(a), validating the theoretical analysis. The oscillations in V_{dc} is reflected in the I_d response, as shown in Fig. 13(b). However, the system remains stable when it operates at the MPP.

D. OPERATION WITH THE PROPOSED COMPENSATOR

The compensator proposed in (51) is added to the system model, and the response is demonstrated in Fig. 14. Compared to the uncompensated response in Fig. 13, the proposed compensator provides a high damping capability in the overall PV-VSC system. As a result, V_{dc} (shown in Fig. 14 (a)) remains stable, and the oscillation frequency changes from 269 to 78.5 rad/s even if the operating point moves, reflecting the effectiveness of the proposed compensator. Moreover, the oscillations in the injected ac currents are reduced, as shown in Fig. 14(b), verifying that the proposed compensator adds positive damping to the system.

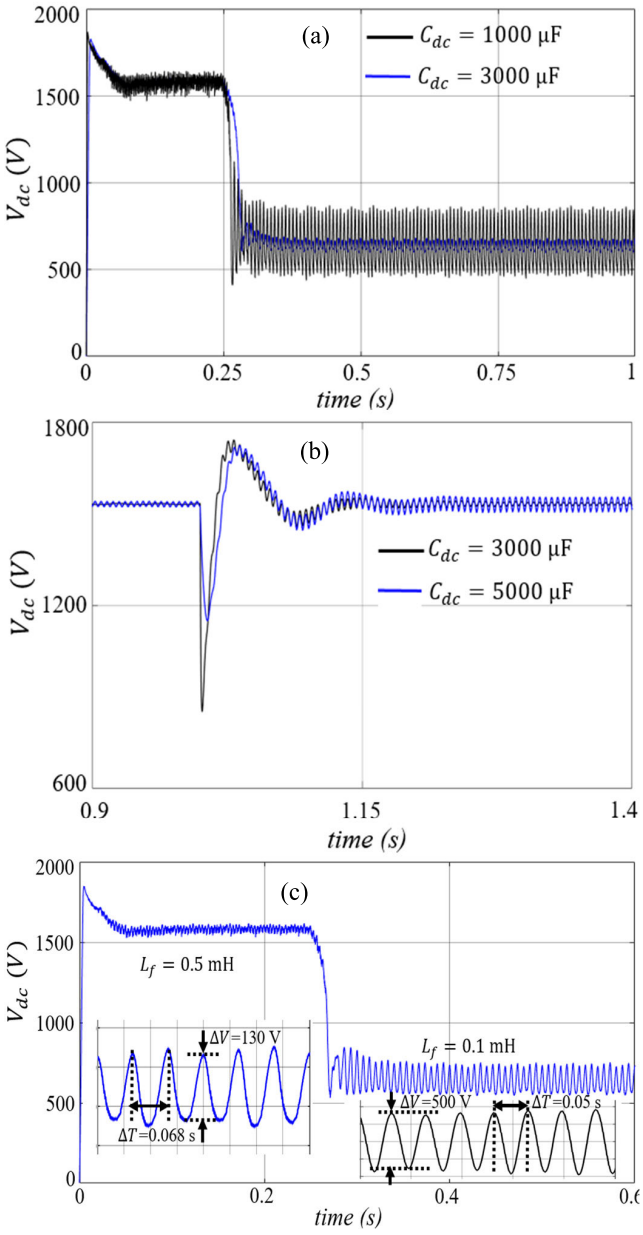

FIGURE 12. Performance under changing parameters: (a) C_{dc}, (b) C_{dc} with disturbance, and (c) L_f.

E. OPERATION UNDER FAULT

A fault (phase A to ground) is introduced at $t = 0.6$ s for 0.2 s at the grid side to investigate the effectiveness of the proposed compensator. The uncompensated V_{dc} response shown in Fig. 15(a) is subjected to undershoot at the fault instant ($t = 0.6$ s) and overshoot once the fault is cleared with a high settling time. The proposed compensator reduces the overshoot in V_{dc} from 1.10 p.u. to 1 p.u. and demonstrates better damping. The proposed compensator also demonstrates better damping against the undershoot, which changes from 0.53 to 0.95 p.u., as shown in Fig. 15(a). The DF-based works already published in the literature did not consider dynamic performance improvement strategies under varying operating points and faults.

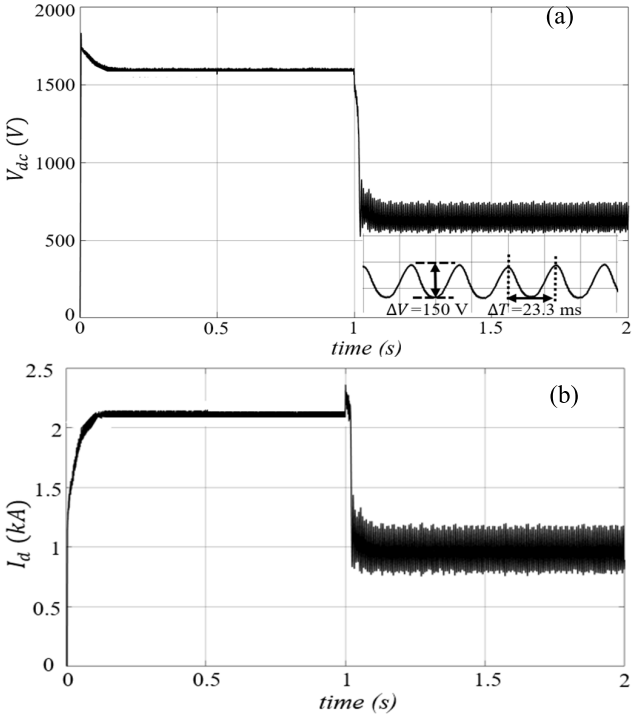

FIGURE 13. Uncompensated response: (a) V_{dc} and (b) I_d.

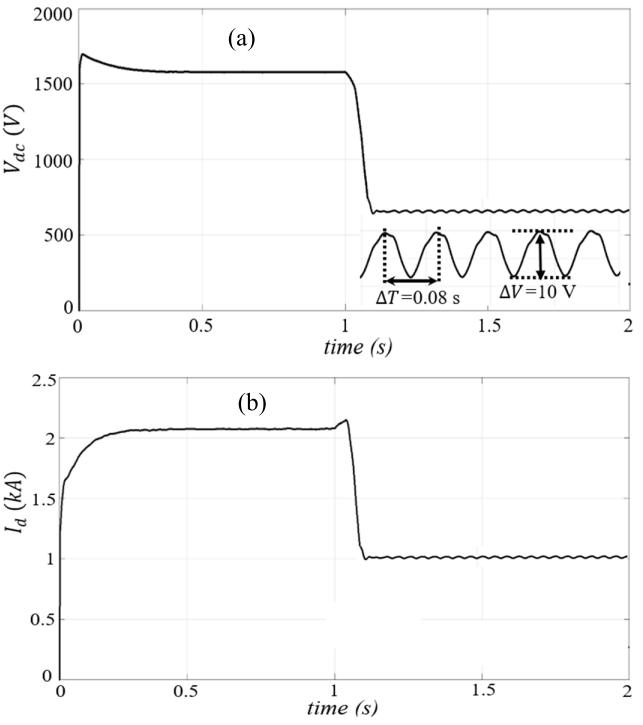

FIGURE 14. Compensated system response: (a) V_{dc} and (b) I_d.

F. OPERATION UNDER GRID-VOLTAGE PARAMETER VARIATION

The phase angle of phase A of the grid voltage is shifted by 30°, and its effect is shown in Fig. 15(b). The uncompensated V_{dc} suffers from an undershoot of 0.8 p.u. and overshoot of 1.03 p.u. at $t = 0.4$ s and $t = 0.6$ s, respectively.

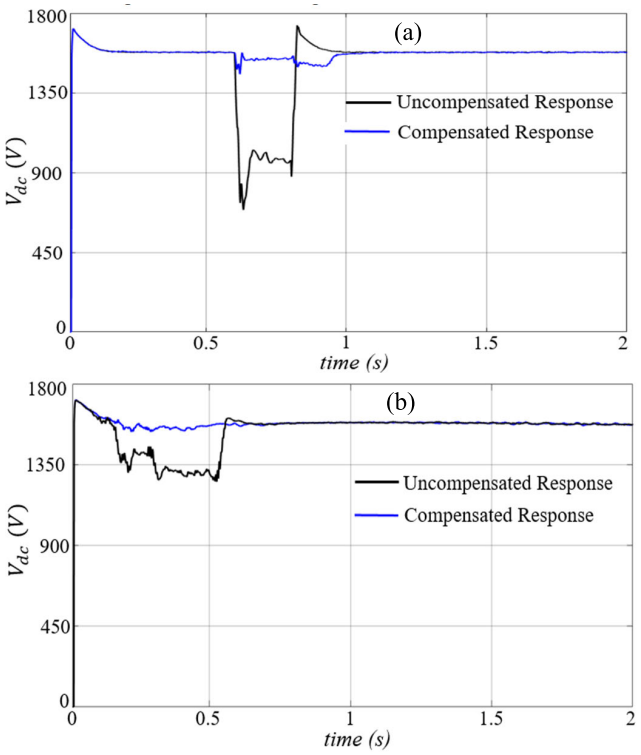

FIGURE 15. DC-link voltage response: (a) fault and (b) grid-voltage phase angle change.

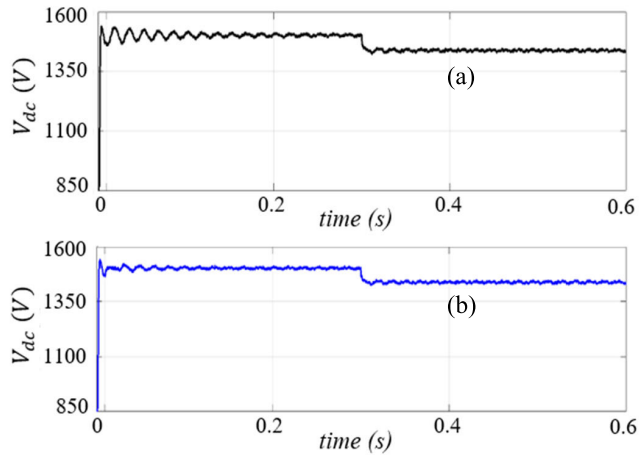

FIGURE 16. Performance under weak grid: (a) Uncompensated and (b) Compensated V_{dc}.

A similar scenario has been applied to the compensated system where a remarkably improved transient response is achieved, as shown in Fig. 15(b), implying the robustness of the proposed compensator against grid-voltage parameter variation.

G. OPERATION UNDER A WEAK GRID CONDITION

The operation and performance investigation of the proposed compensator under a weak grid (short circuit ratio is 2) is evaluated in this section, where the solar insolation level is changed from 1 to 0.6 kW/m^2 at $t = 0.3$ s. Fig. 16(a) shows that uncompensated V_{dc} suffers from higher oscillation under a weak grid condition. However, the compensated response shows a better dynamic performance, as shown in Fig. 16(b), implying increased damping under weak grid conditions.

VIII. CONCLUSION

This paper has presented a comprehensive DF-based nonlinear stability analysis and active compensation method for a utility-scale single-stage grid-connected PV system. First, the INC-based MPPT model is derived and used in the DF-based analysis to characterize the impact of the MPPT sampling time and perturbation step size on oscillation magnitude and frequency. Then, the limit cycle characteristics of the complete system are analyzed under different operating conditions and parameters. Furthermore, a simple yet effective active compensator is proposed to improve the damping and mitigate oscillation under various operating conditions. Finally, detailed time-domain simulation results verify the analytical findings and the effectiveness of the proposed compensator under a wide range of operating conditions. The key findings of this study are summarized as follows.

1) Changes in the INC-based MPPT sampling time and step size significantly affect the oscillatory behavior of the system. A shorter sampling time and larger step size result in a faster response. However, an increase in the step size increases oscillation magnitude; the latter does not change with the sampling time. Therefore, stability studies for grid-connected PV-VSC systems should consider an MPPT parameter-dependent mathematical model for optimal parameter selection and accurate stability assessment.
2) The low-frequency stability is mainly affected by variation in the PVG operating points and reduction in the dc-link capacitance and ac-side filter inductance.
3) The oscillatory behavior in the nonlinear PV-VSC system becomes more evident under grid-side single-line faults, grid-voltage parameter change, and weak grid conditions. Therefore, nonlinear analysis and control are essential to enhance the reliability of grid-connected PV systems.
4) The proposed compensator reshapes the converter dc-side impedance to reduce undesirable interactions with the nonlinear MPPT controller, yielding higher damping capability and reduced oscillations than the uncompensated system.

APPENDIX

A. SYSTEM PARAMETERS

See Tables 1–3.

B. IMPEDANCE CALCULATION

Uncompensated dc-side impedance

$$\Delta Z_{dc} = \frac{V_{dc}^{02}\left(\beta_5 s^5 + \beta_4 s^4 + \beta_3 s^3 + \beta_2 s^2 + \beta_1 s\right)}{\alpha_5 s^5 + \alpha_4 s^4 + \alpha_3 s^3 + \alpha_2 s^2 + \alpha_1 s + \alpha_0}$$

$$\alpha_5 = N^2 L_g L_f C_f \left[1.5 I_d^0 \left(V_{id}^0 + V_{dc}^0 K_p^{vdc} K_i^{vdc}\right) - V_{dc}^0 I_{dc}^0\right]$$

TABLE 1. Parameters of the PV panel and DC-link.

PV and DC-link Parameters	Value	Units
Solar Radiation S	1.0	kW/m^2
Temperature T	298	K
Photo Current I_{ph}	8.24	A
Short Circuit Current I_{sc}	8.23	A
Open Circuit Voltage V_{oc}	30.8	V
PV Module Maximum Current I_{max}	7.71	A
PV Module Maximum Voltage V_{max}	24.7	V
Series Resistance R_s	0.3	Ω
Shunt Resistance R_{sh}	236.4	Ω
Series Module N_s	50	
Parallel String N_p	110	
Cable Resistance R_{dc}	0.163	Ω
Cable Inductance L_{dc}	52.5	μH
DC-link Capacitance C_{dc}	5000	μF

TABLE 2. AC-side parameters.

AC-Side Parameters	Value	Units
VSI Rating P	1.0	MW
Switching Frequency f_{sw}	51*60	Hz
Filter Resistance R_f	2.0	mΩ
Filter Inductance L_f	100	μH
Transformer T_r	11/0.4	kV
Grid Rated Power	36	MVA
Grid Voltage v_{gL-L}	11	kV
Grid Frequency	60	Hz
Grid X/R Ratio	7	

TABLE 3. Control parameters.

Subsystem	Parameter	Value
DC-Side Controller	$G_{vdc}(s)$	$\frac{0.656s+7.2}{s}$
AC-Side Controller	$G_i(s)$	$\frac{0.2s+6}{s}$
PLL Controller	$G_{pll}(s)$	$\frac{0.18s+3.2}{s}$

$$
\begin{aligned}
\alpha_4 &= 1.5\left[N^2L_gC_f\left(V_{id}^0+I_d^0R_f\right)+I_d^0L_fN^2R_gC_f\right]\\
&\quad+\left(V_{id}^0+V_{dc}^0K_p^{vdc}K_p^i\right)+1.5I_d^0N^2L_gL_fV_{dc}^0\\
&\quad\times\left(K_p^{vdc}K_i^i+K_i^{vdc}K_p^i\right)\\
&\quad-V_{dc}^0I_{dc}^0\left[N^2C_f\left(L_gK_p^i+L_gR_f+R_gL_f\right)\right]\\
\alpha_3 &= 1.5I_d^0\left(L_f+N^2L_g\right)\left(V_{id}^0+V_{dc}^0K_p^{vdc}K_p^i\right)\\
&\quad+1.5N^2R_gC_fV_{id}^0\left(V_{id}^0+I_d^0R_f\right)+1.5C_fV_{dc}^0\\
&\quad\times\left[K_p^{vdc}K_p^iN^2R_g\left(V_{id}^0+I_d^0R_f\right)+I_d^0N^2L_gL_fK_i^{vdc}K_i^i\right]\\
&\quad+1.5V_{dc}^0\left(K_p^{vdc}K_i^i+K_i^{vdc}K_p^i\right)\\
&\quad\times\left[N^2L_gC_f\left(V_{id}^0+I_d^0R_f\right)+I_d^0N^2R_gL_fC_f\right]\\
&\quad-V_{dc}^0I_{dc}^0\left[L_f+N^2C_f\left(L_gK_i^i+R_gR_f+R_gK_p^i\right)\right]\\
\alpha_2 &= 1.5I_d^0\left(R_f+N^2R_g\right)\left(V_{id}^0+V_{dc}^0K_p^{vdc}K_p^i\right)+1.5V_{id}^{02}\\
&\quad+1.5V_{id}^0V_{dc}^0\left(K_p^{vdc}K_i^i+K_i^{vdc}K_p^iN^2L_gC_f\right)\\
&\quad+1.5V_{dc}^0\left(K_p^{vdc}K_i^i+K_i^{vdc}K_p^i\right)\\
&\quad\times\left[N^2R_gC_f\left(V_{id}^0+I_d^0R_f\right)+I_d^0\left(L_f+N^2L_g\right)\right]\\
&\quad+1.5I_d^0V_{dc}^0K_i^{vdc}K_i^iN^2C_f\left(L_gR_f+L_fR_g\right)\\
&\quad-V_{dc}^0I_{dc}^0\left(K_p^i+R_f+K_i^iN^2R_gC_f\right)\\
\alpha_1 &= 1.5V_{dc}^0K_i^{vdc}K_i^i\\
&\quad\times\left[N^2R_gC_f\left(V_{id}^0+I_d^0R_f\right)+I_d^0\left(L_f+N^2L_g\right)\right]\\
&\quad+1.5V_{dc}^0\left(K_p^{vdc}K_i^i+K_i^{vdc}K_p^i\right)\\
&\quad\times\left[V_{id}^0+I_d^0\left(R_f+N^2R_g\right)\right]-K_i^iI_{dc}^0V_{dc}^0\\
\alpha_0 &= 1.5V_{dc}^0K_i^{vdc}K_i^i\left[V_{id}^0+I_d^0\left(R_f+N^2R_g\right)\right]\\
\beta_5 &= N^2L_gL_fC_f\\
\beta_4 &= N^2C_f\left(L_gK_p^i+L_gR_f+L_fR_g\right)\\
\beta_3 &= L_f+N^2C_f\left(L_gK_i^i+R_gR_f+R_gK_p^i\right)\\
\beta_2 &= K_p^i+R_f+N^2R_gC_fK_i^i\\
\beta_1 &= K_i^i
\end{aligned}
$$

Compensated dc-side impedance

$$
\begin{aligned}
&\Delta Z_{dc-com}\\
&\quad=\frac{\Delta V_{dc}}{\Delta I_{dc}}\\
&\quad=\frac{V_{dc}^{02}\left(A_6s^6+A_5s^5+A_4s^4+A_3s^3+A_2s^2+A_1s\right)}{B_6s^6+B_5s^5+B_4s^4+B_3s^3+B_2s^2+B_1s+B_0}\\
B_6 &= N^2L_gL_fC_f\left[1.5I_d^0\left(V_{id}^0+V_{dc}^0K_p^{vdc}K_i^{vdc}\right)-V_{dc}^0I_{dc}^0\right]\\
B_5 &= 1.5I_d^0N^2L_gL_fC_f\left[V_{id}^0\omega_c+V_{dc}^0\left(K_p^{vdc}K_i^i+K_p^{vdc}K_p^i\omega_c\right.\right.\\
&\quad\left.\left.+K_p^iK_i^{vdc}-K_p^iK_v\omega_c\right)\right]\\
&\quad+1.5\left[N^2L_gL_f\left(V_{id}^0+I_d^0R_f\right)+I_d^0N^2R_gL_fC_f\right]\\
&\quad\times\left(V_{id}^0+V_{dc}^0K_p^{vdc}K_p^i\right)-V_{dc}^0I_{dc}^0N^2C_f\\
&\quad\times\left[L_g\left(L_f\omega_c+R_g\right)+L_g\left(R_f+K_p^i\right)\right]\\
B_4 &= 1.5I_d^0N^2L_gL_fC_fV_{dc}^0\\
&\quad\times\left[K_i^iK_i^{vdc}+\left(K_p^{vdc}K_i^i+K_i^{vdc}K_p^i-K_i^iK_v\right)\omega_c\right]\\
&\quad+1.5\left[N^2L_gC_f\left(V_{id}^0+I_d^0R_f\right)+I_d^0L_fN^2R_gC_f\right]\\
&\quad\times\left[V_{id}^0\omega_c+V_{dc}^0\left(K_p^{vdc}K_i^i+K_p^{vdc}K_p^i\omega_c\right.\right.\\
&\quad\left.\left.+K_p^iK_i^{vdc}-K_p^iK_v\omega_c\right)\right]\\
&\quad+1.5\left[N^2R_gC_f\left(V_{id}^0+I_d^0R_f\right)+I_d^0\left(L_f+N^2L_g\right)\right]
\end{aligned}
$$

$$\times \left(V_{id}^0 + V_{dc}^0 K_p^{vdc} K_p^i\right) - V_{dc}^0 I_{dc}^0$$
$$\times \left[L_f + N^2 C_f \left\{L_g \omega_c \left(R_f + K_p^i\right) + R_g L_f \omega_c + L_g K_i^i + R_f R_g + R_g K_p^i\right\}\right]$$

$$B_3 = 1.5 I_d^0 N^2 L_g L_f C_f K_i^i K_i^{vdc} V_{dc}^0 \omega_c + 1.5 V_{dc}^0 \left[N^2 L_g C_f \left(V_{id}^0 + I_d^0 R_f\right) + I_d^0 L_f N^2 R_g C_f\right] \times \left[K_i^i K_i^{vdc} + \left(K_p^{vdc} K_i^i + K_i^{vdc} K_p^i - K_i^i K_v\right) \omega_c\right] + 1.5 \left[N^2 R_g C_f \left(V_{id}^0 + I_d^0 R_f\right) + I_d^0 \left(L_f + N^2 L_g\right)\right] \times \left[V_{id}^0 \omega_c + V_{dc}^0 \left(K_p^{vdc} K_i^i + K_p^{vdc} K_p^i \omega_c + K_p^i K_i^{vdc} - K_p^i K_v \omega_c\right)\right] + 1.5 \left[V_{id}^0 + I_d^0 \left(R_f + N^2 R_g\right)\right] \left(V_{id}^0 + V_{dc}^0 K_p^{vdc} K_p^i\right) - V_{dc}^0 I_{dc}^0 \left[L_f \omega_c + N^2 C_f \omega_c \left(L_g K_i^i + R_f R_g + R_g K_p^i\right) + K_p^i + R_f + N^2 R_g C_f K_i^i\right]$$

$$B_2 = 1.5 K_i^i K_i^{vdc} V_{dc}^0 \omega_c \times \left[N^2 L_g C_f \left(V_{id}^0 + I_d^0 R_f\right) + I_d^0 L_f N^2 R_g C_f\right] + 1.5 V_{dc}^0 \left[N^2 R_g C_f \left(V_{id}^0 + I_d^0 R_f\right) + I_d^0 \left(L_f + N^2 L_g\right)\right] \times \left[K_i^i K_i^{vdc} + \left(K_p^{vdc} K_i^i + K_i^{vdc} K_p^i - K_i^i K_v\right) \omega_c\right] + 1.5 \left[V_{id}^0 + I_d^0 \left(R_f + N^2 R_g\right)\right] \times \left[V_{id}^0 \omega_c + V_{dc}^0 \left(K_p^{vdc} K_i^i + K_p^{vdc} K_p^i \omega_c + K_p^i K_i^{vdc} - K_p^i K_v \omega_c\right)\right] - V_{dc}^0 I_{dc}^0 \left[\omega_c \left(K_p^i + R_f + N^2 R_g C_f K_i^i\right) + K_i^i\right]$$

$$B_1 = 1.5 V_{dc}^0 \left[V_{id}^0 + I_d^0 \left(R_f + N^2 R_g\right)\right] \times \left[K_i^i K_i^{vdc} + \left(K_p^{vdc} K_i^i + K_i^{vdc} K_p^i - K_i^i K_v\right) \omega_c\right] + 1.5 K_i^i K_i^{vdc} V_{dc}^0 \omega_c \left[N^2 R_g C_f \left(V_{id}^0 + I_d^0 R_f\right) + I_d^0 \left(L_f + N^2 L_g\right)\right] - V_{dc}^0 I_{dc}^0 K_i^i \omega_c$$

$$B_0 = 1.5 K_i^i K_i^{vdc} V_{dc}^0 \omega_c \left[V_{id}^0 + I_d^0 \left(R_f + N^2 R_g\right)\right]$$

$$A_6 = N^2 L_g L_f C_f$$

$$A_5 = N^2 C_f \left[L_g L_f \omega_c + L_g \left(R_f + K_p^i\right) + R_g L_f\right]$$

$$A_4 = N^2 C_f \left[L_g \omega_c \left(R_f + K_p^i\right) + L_f R_g \omega_c + L_g K_i^i + R_f R_g + R_g K_p^i\right]$$

$$A_3 = L_f \omega_c + N^2 C_f \omega_c \left(L_g K_i^i + R_g R_f + R_g K_p^i\right) + K_p^i + R_f + N^2 R_g C_f K_i^i$$

$$A_2 = \omega_c \left(K_p^i + R_f + N^2 R_g C_f K_i^i\right) + K_i^i$$

$$A_1 = K_i^i \omega_c$$

REFERENCES

[1] Y. Xia, M. Yu, P. Yang, Y. Peng, and W. Wei, "Generation-storage coordination for islanded DC microgrids dominated by PV generators," *IEEE Trans. Energy Convers.*, vol. 34, no. 1, pp. 130–138, Mar. 2019.
[2] B. Guo, M. Su, Y. Sun, H. Wang, B. Liu, X. Zhang, J. Pou, Y. Yang, and P. Davari, "Optimization design and control of single-stage single-phase PV inverters for MPPT improvement," *IEEE Trans. Power Electron.*, vol. 35, no. 12, pp. 13000–13016, Dec. 2020.
[3] F.-J. Lin, K.-C. Lu, and B.-H. Yang, "Recurrent fuzzy cerebellar model articulation neural network based power control of a single-stage three-phase grid-connected photovoltaic system during grid faults," *IEEE Trans. Ind. Electron.*, vol. 64, no. 2, pp. 1258–1268, Feb. 2017.
[4] Y. Xia, Y. Peng, P. Yang, Y. Li, and W. Wei, "Different influence of grid impedance on low- and high-frequency stability of PV generators," *IEEE Trans. Ind. Electron.*, vol. 66, no. 11, pp. 8498–8508, Nov. 2019.
[5] A. Yazdani and P. P. Dash, "A control methodology and characterization of dynamics for a photovoltaic (PV) system interfaced with a distribution network," *IEEE Trans. Power Del.*, vol. 24, no. 3, pp. 1538–1551, Jul. 2009.
[6] T. Messo, J. Jokipii, J. Puukko, and T. Suntio, "Determining the value of DC-link capacitance to ensure stable operation of a three-phase photovoltaic inverter," *IEEE Trans. Power Electron.*, vol. 29, no. 2, pp. 665–673, Feb. 2014.
[7] V. M. Lyer and V. John, "Low-frequency DC bus ripple cancellation in single phase pulse-width modulation inverters," *IET Power Electron.*, vol. 8, no. 4, pp. 497–506, Apr. 2015.
[8] F. E. Aamri, H. Maker, D. Sera, S. Spataru, J. M. Guerrero, and A. Mouhsen, "A direct maximum power point tracking method for single-phase grid-connected PV inverters," *IEEE Trans. Power Electron.*, vol. 33, no. 10, pp. 8961–8971, Oct. 2018.
[9] S. K. Kollimalla and M. K. Mishra, "Variable perturbation size adaptive P&O MPPT algorithm for sudden changes in irradiance," *IEEE Trans. Sustain. Energy*, vol. 5, no. 3, pp. 718–728, Jul. 2014.
[10] D. Sera, L. Mathe, T. Kerekes, S. V. Spataru, and R. Teodorescu, "On the perturb-and-observe and incremental conductance MPPT methods for PV systems," *IEEE J. Photovolt.*, vol. 3, no. 3, pp. 1070–1078, Jul. 2013.
[11] G. Escobar, S. Pettersson, C. N. M. Ho, and R. Rico-Camacho, "Multisampling maximum power point tracker (MS-MPPT) to compensate irradiance and temperature changes," *IEEE Trans. Sustain. Energy*, vol. 8, no. 3, pp. 1096–1105, Jul. 2017.
[12] Z. Moradi-Shahrbabak and A. Tabesh, "Effects of front-end converter and DC-link of a utility-scale PV energy system on dynamic stability of a power system," *IEEE Trans. Ind. Electron.*, vol. 65, no. 1, pp. 403–411, Jan. 2018.
[13] S. Liu, P. X. Liu, and X. Wang, "Stochastic small-signal stability analysis of grid-connected photovoltaic systems," *IEEE Trans. Ind. Electron.*, vol. 63, no. 2, pp. 1027–1038, Feb. 2016.
[14] Z. Zhao, P. Yang, Y. Wang, Z. Xu, and J. M. Guerrero, "Dynamic characteristics analysis and stabilization of PV-based multiple microgrid clusters," *IEEE Trans. Smart Grid*, vol. 10, no. 1, pp. 805–818, Jan. 2019.
[15] G. J. Kish, J. J. Lee, and P. W. Lehn, "Modelling and control of photovoltaic panels utilising the incremental conductance method for maximum power point tracking," *IET Renew. Power Gener.*, vol. 6, no. 4, pp. 259–266, Jul. 2012.
[16] N. Femia, G. Petrone, G. Spagnuolo, and M. Vitelli, "A technique for improving P&O MPPT performances of double-stage grid-connected photovoltaic systems," *IEEE Trans. Ind. Electron.*, vol. 56, no. 11, pp. 4473–4482, Nov. 2009.
[17] M. A. Elgendy, B. Zahawi, and D. J. Atkinson, "Assessment of the incremental conductance maximum power point tracking algorithm," *IEEE Trans. Sustain. Energy*, vol. 4, no. 1, pp. 108–117, Jan. 2013.
[18] N. Femia, G. Petrone, G. Spagnuolo, and M. Vitelli, "Optimization of perturb and observe maximum power point tracking method," *IEEE Trans. Power Electron.*, vol. 20, no. 4, pp. 963–973, Jul. 2005.
[19] S. Liu, P. X. Liu, and X. Wang, "Stability analysis of grid-interfacing inverter control in distribution systems with multiple photovoltaic-based distributed generators," *IEEE Trans. Ind. Electron.*, vol. 63, no. 12, pp. 7339–7348, Dec. 2016.
[20] M. Davari and Y. A.-R. I. Mohamed, "Robust vector control of a very weak-grid-connected voltage-source converter considering the phase-locked loop dynamics," *IEEE Trans. Power Electron.*, vol. 32, no. 2, pp. 977–994, Feb. 2017.
[21] M. A. Mahmud, H. R. Pota, and M. J. Hossain, "Dynamic stability of three-phase grid-connected photovoltaic system using zero dynamic design approach," *IEEE J. Photovolt.*, vol. 2, no. 4, pp. 564–571, Oct. 2012.

[22] Y. Huang, X. Yuan, J. Hu, and P. Zhou, "Modeling of VSC connected to weak grid for stability analysis of DC-link voltage control," *IEEE J. Emerg. Sel. Topics Power Electron.*, vol. 3, no. 4, pp. 1193–1204, Dec. 2015.
[23] Y. Gu, W. Li, and X. He, "Passivity-based control of DC microgrid for self-disciplined stabilization," *IEEE Trans. Power Syst.*, vol. 30, no. 5, pp. 2623–2632, Sep. 2015.
[24] Y. Xia, M. Yu, X. Wang, and W. Wei, "Describing function method based power oscillation analysis of LCL-filtered single-stage PV generators connected to weak grid," *IEEE Trans. Power Electron.*, vol. 34, no. 9, pp. 8724–8738, Sep. 2019.
[25] W. Wei, Y. Xia, and F. Blaabjerg, "Nonlinear stability analysis for three-phase grid-connected PV generators," *IEEE J. Emerg. Sel. Topics Power Electron.*, vol. 8, no. 4, pp. 3487–3501, Dec. 2020.
[26] V. Jain and B. Singh, "A multiple improved notch filter-based control for a single-stage PV system tied to a weak grid," *IEEE Trans. Sustain. Energy*, vol. 10, no. 1, pp. 238–247, Jan. 2019.
[27] L. B. G. Campanhol, S. A. O. da Silva, A. A. de Oliveira, and V. D. Bacon, "Single-stage three-phase grid-tied PV system with universal filtering capability applied to DG systems and AC microgrids," *IEEE Trans. Power Electron.*, vol. 32, no. 12, pp. 9131–9142, Dec. 2017.
[28] A. A. A. Radwan and Y. A.-R.-I. Mohamed, "Grid-connected wind-solar cogeneration using back-to-back voltage-source converters," *IEEE Trans. Sustain. Energy*, vol. 11, no. 1, pp. 315–325, Jan. 2020.
[29] D. Engels, "The describing functions for a constrained-range integration process with bang-bang input and dead zone," *IEEE Trans. Autom. Control*, vol. AC-12, no. 5, pp. 582–585, Oct. 1967.
[30] Y. Xu, Z. Gu, and K. Sun, "Characterization of subsynchronous oscillation with wind farms using describing function and generalized Nyquist criterion," *IEEE Trans. Power Syst.*, vol. 35, no. 4, pp. 2783–2793, Jul. 2020.
[31] Y. Xia, W. Wei, M. Yu, and P. Wang, "Stability analysis of PV generators with consideration of P&O-based power control," *IEEE Trans. Ind. Electron.*, vol. 66, no. 8, pp. 6483–6492, Aug. 2019.
[32] H. Li, J. Shang, B. Zhang, X. Zhao, N. Tan, and C. Liu, "Stability analysis with considering the transition interval for PWM DC–DC converters based on describing function method," *IEEE Access*, vol. 6, pp. 48113–48124, Jul. 2018.
[33] H. Li, S. Wang, J. Lü, X. You, and X. Yu, "Stability analysis of the shunt regulator with nonlinear controller in PCU based on describing function method," *IEEE Trans. Ind. Electron.*, vol. 64, no. 3, pp. 2044–2053, Mar. 2017.
[34] A. A. A. Radwan and Y. A.-R. I. Mohamed, "Analysis and active suppression of AC- and DC-side instabilities in grid-connected current-source converter-based photovoltaic system," *IEEE Trans. Sustain. Energy*, vol. 4, no. 3, pp. 630–642, Jul. 2013.
[35] *PV-UD190MF5*, Mitsubishi, San Francisco, CA, USA, 2007.
[36] A. Yazdani and R. Iravani, *Voltage-Sourced Converters in Power Systems: Modeling, Control, and Application*. Hoboken, NJ, USA: Wiley, 2010.

MD. MIZANUR RAHMAN (Member, IEEE) received the B.Sc. degree in electrical and electronic engineering from the Chittagong University of Engineering and Technology, Chittagong, Bangladesh, in August 2011, and the M.Sc. degree in electrical and computer engineering from Lakehead University, Thunder Bay, ON, Canada, in May 2016. He is currently pursuing the Ph.D. degree in electrical and computer engineering with the University of Alberta, Edmonton, AB, Canada.

He worked as a Lecturer with the Electrical and Computer Engineering Department, North South University, Dhaka, Bangladesh, from January 2017 to August 2018. His research interests include stability analysis and control of renewable energy sources and their integration into distribution networks, dc grids, and control of motor drives.

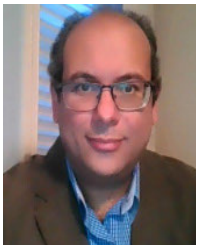

YASSER ABDEL-RADY I. MOHAMED (Fellow, IEEE) was born in Cairo, Egypt, in November 1977. He received the B.Sc. (Hons.) and M.Sc. degrees in electrical engineering from Ain Shams University, Cairo, in 2000 and 2004, respectively, and the Ph.D. degree in electrical engineering from the University of Waterloo, Waterloo, ON, Canada, in 2008.

He is currently a Professor with the Department of Electrical and Computer Engineering, University of Alberta, Edmonton, AB, Canada. His research interests include dynamics and controls of power converters, grid integration of distributed generation and renewable resources, microgrids, modeling, analysis, and control of smart grids, and electric machines and motor drives.

Dr. Mohamed is an Associate Editor of the IEEE TRANSACTIONS ON POWER ELECTRONICS and an Editor of the IEEE TRANSACTIONS ON POWER SYSTEMS, IEEE TRANSACTIONS ON SMART GRID, and IEEE POWER ENGINEERING LETTERS. He is a Registered Professional Engineer in the Province of Alberta.